

The role of primary and secondary electrons in scanning transmission electron microscopy of hybrid perovskites: the CsPbBr₃ case.

P. E. Trevisanutto,¹ S. Taioli,^{2,3} M. Dapor,^{2,3} C. S. Allen,^{4,5} and G. Teobaldi⁶

¹*Scientific Computing Department, STFC UKRI, Daresbury Laboratory, Warrington WA4 4AD, United Kingdom**

²*European Centre for Theoretical Studies in Nuclear Physics and Related Areas (ECT*), Bruno Kessler Foundation, Trento, Italy*

³*Trento Institute for Fundamental Physics and Applications (TIFPA), Istituto Nazionale di Fisica Nucleare, Italy*

⁴*Electron Physical Science Imaging Center, Diamond Light Source Ltd., Didcot OX11 0DE, United Kingdom*

⁵*Department of Materials, University of Oxford, Oxford OX1 3PH, United Kingdom*

⁶*Scientific Computing Department, STFC UKRI, Rutherford Appleton Laboratory, Didcot OX11 0QX, United Kingdom*

High-resolution imaging has revolutionized materials science by offering detailed insights into the atomic structures of materials. Electron microscopy and spectroscopy rely on analysing backscattered and transmitted electrons as well as stimulated radiation emission to form structural and chemical maps. These signals contain information about the elastic and inelastic electron-scattering processes within the sample, including collective and single electron excitations such as plasmons, inter- and intraband transitions. In this study, ab initio and Monte Carlo simulations were performed to investigate the behaviour of high-energy primary and secondary electrons in scanning transmission experiments on CsPbBr₃ nanosamples. CsPbBr₃ is a perovskite material known for its high photoluminescence quantum yield, making it promising for applications in light-emitting devices and solar cells. This study explores and estimates the reflection and transmission of primary and secondary electrons based on their kinetic energy as well as sample thickness and work function. The spatial distribution and energy spectra of the secondary electrons are also examined and calculated to understand their generation depth and energy dynamics. These findings establish a theoretical framework for studying electron-material interactions and can aid in optimizing scanning microscopy techniques for imaging and characterizing advanced materials.

I. INTRODUCTION

Among the significant advances in analytical techniques for materials science, atomic resolution imaging is one of the most impactful. These methods have enabled detailed visualisation of the structures and morphology of nanomaterials, crystals and metal surfaces, as well as biological samples and tissues [1, 2].

In transmission electron microscopy (TEM), a beam of high-energy electrons (typically 80-300 keV) is passed through a very thin sample (~ 100 nm) and interference between elastically scattered electrons is exploited to form an image. This approach enables a high resolution imaging down to the atomic resolution (~ 0.1 nm) and allows the precise visualisation of atomic arrangements. In a scanning electron microscope (SEM) a focused beam of electrons is raster scanned across a sample and nm resolution images of the surface are formed from the analysis of emitted secondary electrons (SE) and backscattered electrons (BSE). The resolution in a SEM is largely limited by the interaction volume of the detected radiation which, in most cases, precludes the need for incident electron probes smaller than ~ 1 nm. Scanning transmission electron microscopy (STEM) combines elements of SEM and TEM. A finely focused electron beam is raster scanned across a thin sample (~ 100 nm), and elastically scattered electrons are detected to form an image. At high incident electron energy and for thin samples, the interaction volume for elastic scattering is small and the microscope resolution is primarily limited by the size of the incident electron probe, which with modern aberration-corrected optics can reach sub-Ångström dimensions. Together with other emissions such as Auger electrons which are used to characterise the surface elemental compositions and X-rays applied to determine bulk crystal structures, the SEM, TEM and STEM represent the main techniques to analyse chemical composition and structure [3].

In high-resolution STEM and TEM experiments a projection image is acquired and it is challenging to obtain information on sample variation along the beam direction. By placing SE detectors both before and after the sample within a STEM instrument, the surface sensitivity of SE detection can be exploited to determine structure on the entrance and exit surfaces of a thin sample [4, 5], to some extent overcoming the projection limitation of the STEM.

A recent review [6], has highlighted the applications for studying the dynamics and transient phenomena of surface reconstructions, exsolution of catalysts, lunar and planetary materials and mechanical properties of 2D thin films

* paolo.trevisanutto@stfc.ac.uk

utilising the simultaneous SE-STEM imaging.

Furthermore, inelastic scattering events within the sample, including SE generation [7] are a primary cause of electron beam-induced sample damage and need to be well understood to help develop novel approaches to imaging beam-sensitive materials.

Motivated by the potential for transmitted SE imaging described in the above works, we construct a theoretical framework to calculate SE generation and emission in transmission through an industrially relevant metal-halide perovskite sample.

Any electron microscopy technique relies on electron scattering in the sample, which includes both elastic and inelastic processes. Both spectroscopic and SE imaging are products of inelastic scattering processes within the sample. These mechanisms are driven by energy loss phenomena, including single-particle electron excitations, collective atomic modes such as plasmons, electron-phonon and electron-polaron interactions, and Auger decay. Part of the energy loss contributes to the generation of a secondary electron cascade and, upon emission from the surface, to the secondary electron yield (SEY). Secondary electrons appear in the electron energy spectrum as a tail with energies below 50 eV. The emission of secondary electrons in SEM plays a decisive role in the formation of the image contrast [8] and can also lead to unwanted charging of the sample, for example, [9].

Electron energy loss phenomena are influenced by two factors, namely the properties of the beam (i.e. kinetic energy, radiation type and charge state) and the material properties, in particular the electronic excitation spectrum. The latter can be described by the so-called energy loss function (ELF), which can be obtained either from optical experiments or from EELS using a single scattering spectrum in which the elastic peak and multiple scattering have been removed [10] or via a Reverse Monte Carlo (RMC) method [11]. The ELF is a unique property of the material and is independent of the beam. However, it is difficult to interpret this from the experiment alone since the uniqueness of the ELF is not guaranteed by the fulfilment of the sum rules, i.e. the EELS signal can lead to different ELF's that all fulfil the sum rules [12] and thus to different beam stopping properties. This emphasises the need for more precise theoretical descriptions and predictions of electron energy loss. In this context, *ab initio* calculations can also be used to determine the dielectric properties, especially in the low energy loss region.

In this article, the scattering behaviour of high-energy primary (up to 50 keV) and secondary (up to 50 eV) electrons in STEM experiments on CsPbBr₃ thin films is investigated theoretically using mixed first-principles calculations and Monte Carlo (MC) approach. In particular, the linear response time-dependent density functional theory (LR-TDDFT) is used to calculate the ELF, while the charge transport in solids is modelled by an MC routine. We have also investigated the reflection and transmission of primary and secondary electrons as a function of the kinetic energy of incidence and the sample thickness. Since electron microscopy (EM) samples are susceptible to beam-inducing charging, we also determined the effects of the work function (WF) on electron emission. Finally, we determined the SE spectra and spatial distribution as a function of the initial kinetic energy of the primary beam by calculating the depth of secondary electron generation.

Caesium lead bromide, CsPbBr₃, is an inorganic perovskite material that has attracted much attention in optoelectronics due to its high photoluminescence quantum yield (PLQY) with a sharp, narrow-band blue-green light emission [13–18]. These properties make it a good candidate for industrial applications, e.g. in light-emitting devices (LEDs). As CsPbBr₃ is a purely inorganic material, it is more stable under heat and less susceptible to degradation under harsh environmental conditions [19–21]. Although CsPbBr₃ has a relatively large bandgap (about 2.3 eV [22]), it can be used in tandem solar cells alongside silicon or other materials to cover different parts of the solar spectrum and increase overall efficiency. In addition, CsPbBr₃ exhibits the “hot carrier effect” [23, 24], in which excited electrons maintain high energy levels longer than in other materials, which has the potential to further increase the efficiency of solar cells.

II. THEORY AND METHODS

A. Energy Loss Function

The energy loss processes of electrons are described using Ritchie’s dielectric theory [25, 26]. This approach is based on the knowledge of the macroscopic dielectric function $\bar{\epsilon}(\mathbf{q}, \omega)$, which can be calculated from first-principles using linear-response time-dependent density functional theory (LR-TDDFT) or obtained from optical experiments. The former allows the inclusion of momentum dispersion, which is necessary for the calculation of the stopping properties of materials, with the same computational effort as in zero-momentum transfer, while the latter approach must be extended to finite momentum by analytical dispersion laws, which are known to be valid only within certain limits [26]. We have considered the orthorhombic geometric structure of CsPbBr₃ [22, 27] shown in Fig. 1.

The electronic structure in the ground state was relaxed using the generalised gradient approximation (GGA) of the exchange-correlation functional as implemented in QE, Elk and Questaal. We have checked the convergence of

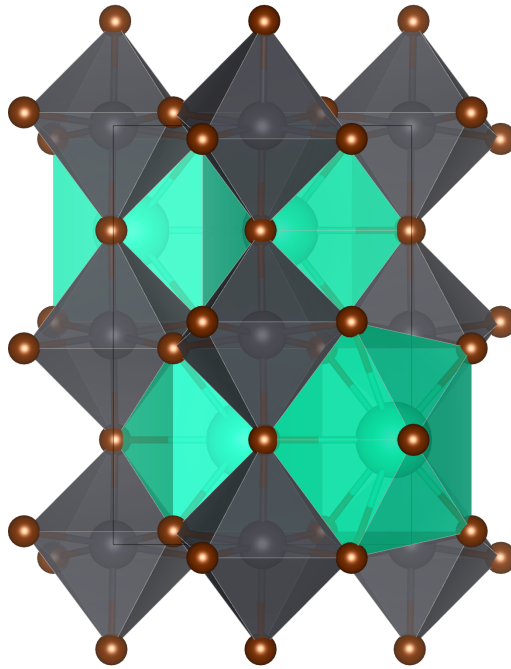


FIG. 1: Geometric structure of CsPbBr₃ optimised by using Density Functional Theory

the DFT parameters given in the literature [27]. We point out that the DFT and LR-TDDFT calculations performed with QE, Elk and Questaal were carried out within the random-phase approximation neglecting local field effects (RPA-NLFE). We have converged our k -mesh grid up to $21 \times 21 \times 21$ points. The ALDA and RPA-LFE LR-TDDFT calculations were performed with the turboEELS code [28]. In the LR-TDDFT, the susceptibility function $\chi(\mathbf{q}, \omega)$ can be obtained by solving the following Dyson-like equation:

$$\chi(\mathbf{q}, \omega)^{-1} = \chi(\mathbf{q}, \omega)_0^{-1} - v_C(\mathbf{q}) - f_{xc}(\mathbf{q}, \omega), \quad (1)$$

where \mathbf{q} is the momentum transfer vector, ω is the absorbed energy, $\chi(\mathbf{q}, \omega)_0$ is the non-interacting (or independent) particle susceptibility calculated from the Kohn-Sham wave functions and $v_C(\mathbf{q})$ is the Coulomb potential. In this work, we used the Adiabatic Local Density Approximation (ALDA) [29] to calculate the TDDFT kernel $f_{xc}(\mathbf{q}, \omega)$. The microscopic dielectric function $\epsilon(\mathbf{q}, \omega)$ of the material is related to the susceptibility as follows:

$$\epsilon(\mathbf{q}, \omega) = 1 - v_C(\mathbf{q})\chi(\mathbf{q}, \omega). \quad (2)$$

In a periodic crystal, the microscopic dielectric function is denoted in reciprocal space as $\epsilon_{\mathbf{G}, \mathbf{G}'}(\mathbf{q}, \omega) \equiv \epsilon(\mathbf{q} + \mathbf{G}, \mathbf{q} + \mathbf{G}', \omega)$, where \mathbf{G} and \mathbf{G}' are reciprocal lattice vectors. The macroscopic dielectric function (or dielectric matrix) $\bar{\epsilon}$ is related to the microscopic dielectric function by the following expression:

$$\bar{\epsilon}(\mathbf{q}, \omega) = [\epsilon^{-1}]_{\mathbf{G}=0, \mathbf{G}'=0}^{-1}(\mathbf{q}, \omega). \quad (3)$$

If this relationship is applied to the momentum in the first Brillouin zone $\mathbf{q} \rightarrow 0$ is referred to as the “optical limit”. The inversion of ϵ^{-1} with \mathbf{G} and \mathbf{G}' not equal to zero leads to the inclusion of the so-called local field effects (LFE), which take into account the inhomogeneity of the system, in contrast to the non-local field effect (NLFE), in which only the head of the matrix is inverted. The ELF can be written as:

$$\text{ELF} \equiv -\text{Im}(\bar{\epsilon}^{-1}) = \frac{\text{Im} \bar{\epsilon}}{\text{Im} \bar{\epsilon}^2 + \text{Re} \bar{\epsilon}^2}. \quad (4)$$

To determine the effects of the ALDA correlation, the random phase approximation (RPA) to $f_{xc}(\mathbf{q}, \omega) = 0$ is also used within LFE and NLFE. In the upper graph of Fig. (2) the ELFs are compared in the context of ALDA, RPA-LFE and RPA-NLFE. Since we are currently not able to compare our computer simulations with the experimental

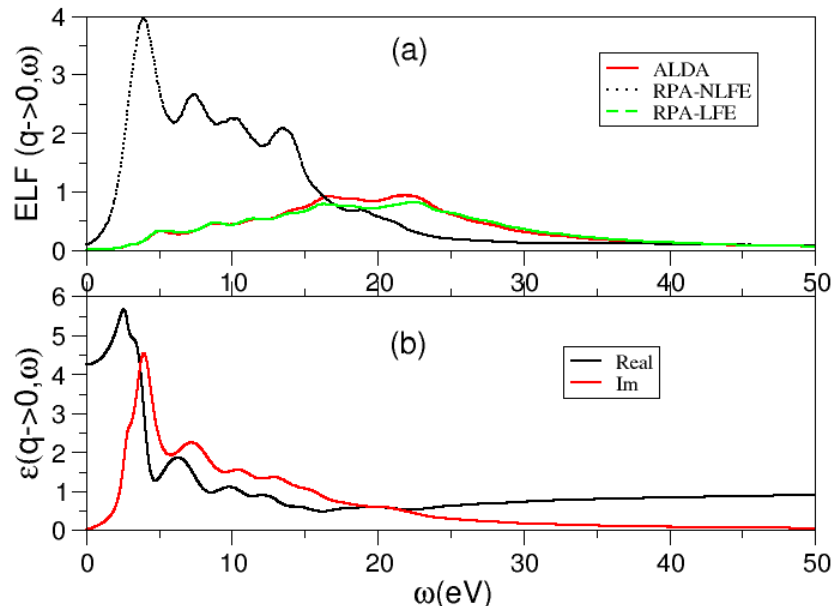


FIG. 2: (a) $\text{ELF}(\mathbf{q} \rightarrow 0)$ of CsPbBr_3 in NLFE-RPA (dotted black line), LFE-RPA (dashed green line) and ALDA (red solid line). (b) The real (black solid line) and imaginary (red solid line) parts of the dielectric function are calculated using LR-TDDFT within the ALDA framework.

results, the peaks are convolved with a typical Gaussian broadening of 0.1 eV. When RPA-LFE is compared with RPA-NLFE, a dramatic change in the shape of the ELF can be observed due to the inhomogeneities. At the same time, the electron correlation in the ALDA kernel slightly increases the intensity in the 15-25 eV range, especially the 16.75 and ~ 22 eV peaks, compared to RPA-LFE. The first less bright peak at 5 eV in the ALDA and RPA-LFE spectra is associated with the transition from the $4p$ states of the Br atom to the $6p$ states of Pb. The rich peak structures beyond 6 eV are primarily caused by transitions from the $4p$ states of the Br atom to a combination of $6p$ states of Cs and $6p$ states of Pb.

The imaginary and real parts of the dielectric matrix are shown in the bottom panel of Fig. (2). By analysing their spectral behaviour, it can be concluded that the 22 eV peak is associated with a mixed-state plasmon (the real part of the dielectric function remains positive, even if it is almost zero). In Fig. (3), the TD-DFT ALDA ELF is merged with the experimental form factors from the NIST datasets [30]. This merging approach is due to the fact that high-energy TD-DFT ELF estimation is computationally too demanding due to the occurrence of numerous excited states. On the other hand, the extension from 100 eV to 400 keV, which is related to the atomic core-level excitations, is needed to accurately determine the total inelastic cross-section.

B. Total inelastic scattering cross-section and mean free path

To calculate the differential inverse inelastic mean free path (DIIMFP), which is used in our MC algorithm, we need to extend the ELF in the optical limit to finite momentum transfer \mathbf{q} to account for energy-momentum dispersion. We have opted for the Drude-Lorentz approximation, where the dispersion is typically assumed to be a square law [26] (see Appendix for details). The equation for the inverse inelastic mean free path (IIMFP), from which the total inelastic scattering cross-section can be derived, is given by

$$\lambda_{\text{inel}}^{-1}(E) = \frac{1}{E\pi a_0} \int_{W_{\text{min}}}^{W_{\text{max}}} d\omega \int_{q_-}^{q_+} \frac{dq}{q} \text{Im} \left[-\frac{1}{\bar{\epsilon}(q, \omega)} \right], \quad (5)$$

where the lower and upper limits of the integral $q_{\pm} = \sqrt{2mE} \pm \sqrt{2m(E - \hbar\omega)}$ are obtained by the energy-momentum conservation laws, W_{min} is the band gap, W_{max} corresponds to the maximum energy of the incident electrons, a_0 is

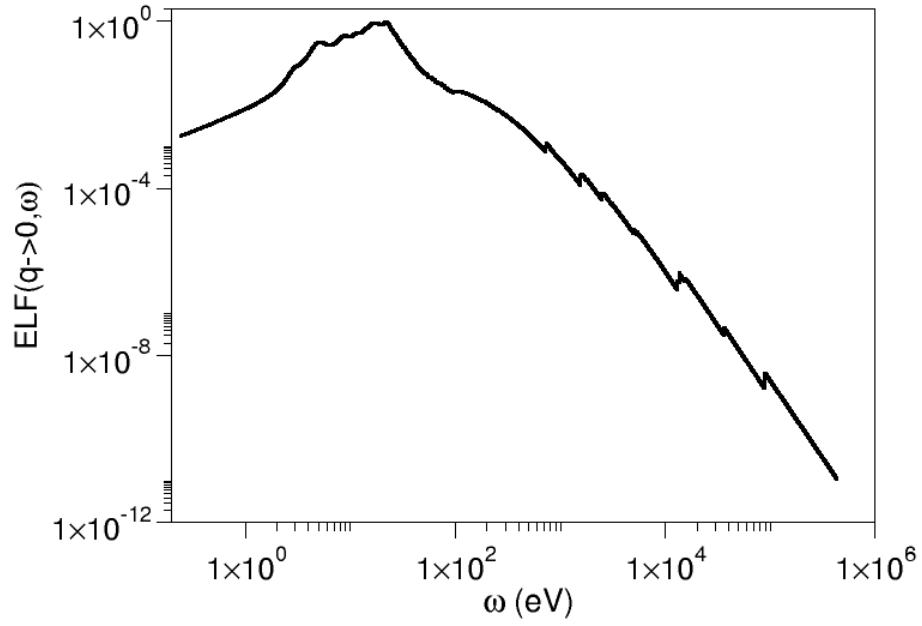


FIG. 3: ELF of CsPbBr₃ in LR-TDDFT ALDA merged with the ELF derived from the experimental form factors of the NIST datasets [30]

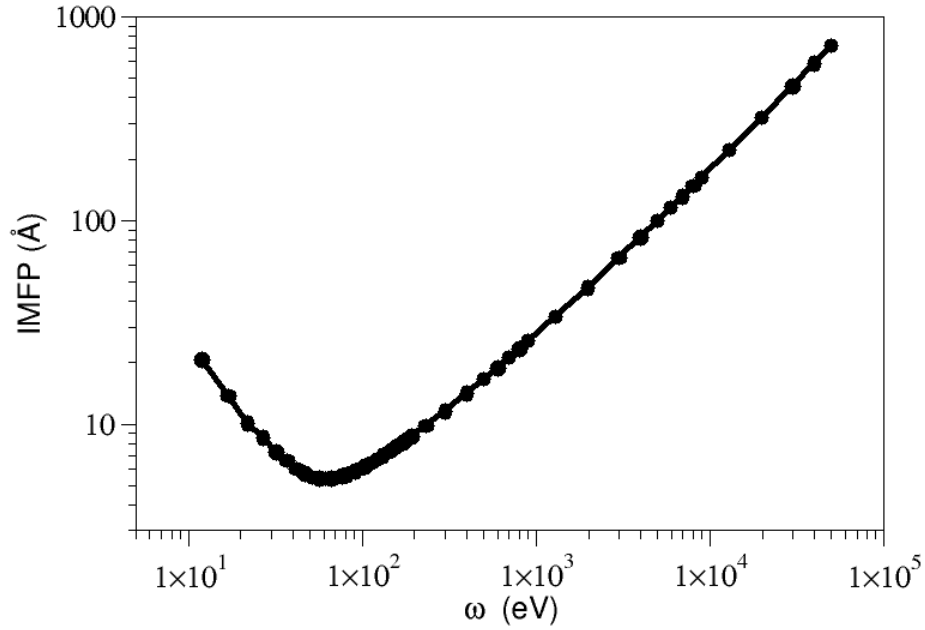


FIG. 4: IMFP (\AA) as a function of the kinetic energy of the incident electron (eV), obtained by extending the ELF from TDDFT-ALDA in the energy axis via the NIST datasets and in the momentum transfer axis \mathbf{q} according to the Drude-Lorentz dispersion law. The minimum of the IMFP is 5.34 \AA for an energy of 57 eV

the Bohr radius and m is the electron mass. Figure (4) shows the IMFP (λ_{inel}) for CsPbBr₃ as a function of the electron kinetic energy. The IMFP minimum is reached at 5.34 Å for an incident electron energy of 57 eV.

C. Total elastic scattering cross-section and mean free path

Elastic scattering is accounted for in our MC approach using Mott theory, which we have generalised to account for the presence of multiple scattering between neighbours in the periodic unit cell [31]. In this approach, the differential elastic scattering cross-section (DESCS) for an electron scattered by a central atomic potential at an angle θ is as follows:

$$\frac{d\sigma_{\text{el}}(E, \theta)}{d\Omega} = \sum_{m,n} e^{i\mathbf{q}\cdot\mathbf{r}_{m,n}} [f_m(\theta)f_n^*(\theta) + g_m(\theta)g_n^*(\theta)], \quad (6)$$

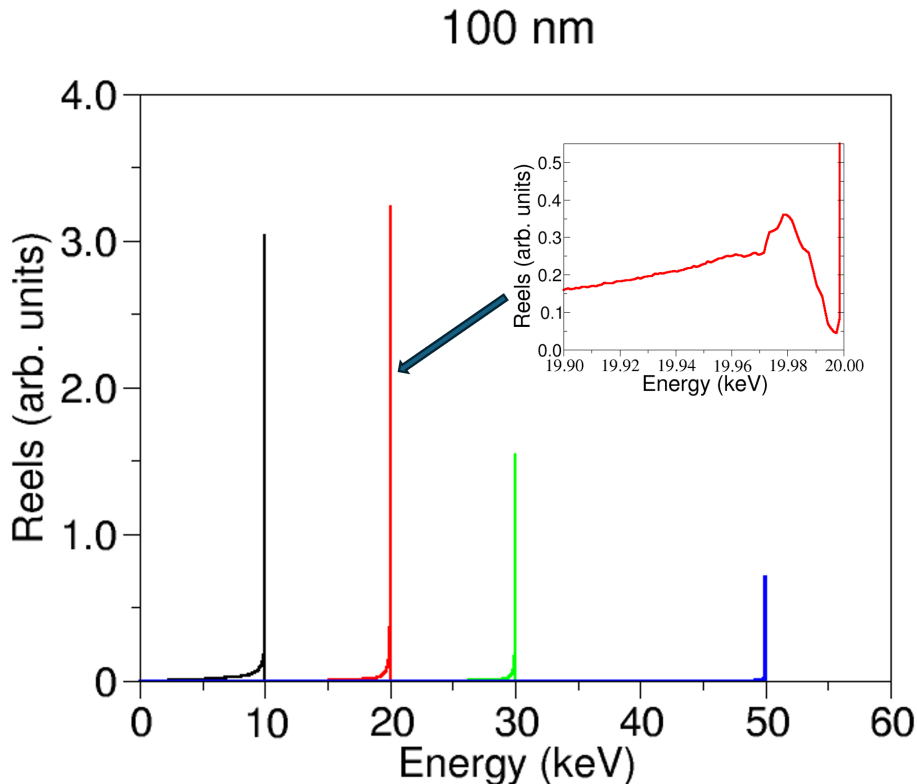


FIG. 5: Monte Carlo simulation of the energy loss spectrum of electrons emerging from a 100 nm thick CsPbBr₃ sample for different kinetic energies of the primary beam: 10 (black line), 20 (red line), 30 (green line) and 50 (blue line) keV. The inset shows the plasmon peak for a 20 keV electron beam.

where $f_m(\theta)$ and $g_m(\theta)$ are the Mott amplitudes of the direct and spin-flip scattering for the m, n atoms, which were determined using the relativistic partial wave expansion method [26] and $\mathbf{r}_{m,n} = \mathbf{r}_m - \mathbf{r}_n$ indicates the distance between the m th and n th atom. θ and Ω are the scattering and solid angles, respectively, measured in the laboratory frame. The total elastic scattering cross-section integrated over Ω results as:

$$\sigma_{\text{el}}(E) = \int_{\Omega} \frac{d\sigma_{\text{el}}(E, \theta)}{d\Omega'} d\Omega'. \quad (7)$$

III. MONTE CARLO RESULTS

Since we have access to the cross sections of elastic and inelastic scattering, our MC algorithm works as follows [26, 32]: We extract a random number μ that is sampled from a uniform distribution in the interval $[0, 1]$ and use it to determine the step length that each electron travels within the solid target $\Delta s = -\lambda \ln(\mu)$, where λ is the mean free path that includes all elastic (λ_{el}^{-1}) and inelastic ($\lambda_{\text{inel}}^{-1}$) scattering processes and can be calculated from $\lambda^{-1} = \lambda_{\text{el}}^{-1} + \lambda_{\text{inel}}^{-1}$. Finally, the MC method selects an elastic or inelastic scattering event by comparing another random number μ' , which is sampled from a uniform distribution in the range $[0, 1]$, with the corresponding probability. If $\mu' \leq \lambda_{\text{el}}^{-1} / \lambda^{-1}$, it is an elastic scattering event that leads to an angular deviation of the electron's trajectory, otherwise, the electron suffers an inelastic interaction that leads to both energy loss and (small) angular deviation [32]. We note that in order to escape from the surface of the sample, the electrons must overcome the barrier at the interface between the vacuum and the solid, i.e. they must fulfil the condition $E \cos^2(\vartheta) \geq \text{WF}$ where ϑ is the angle formed between the surface normal and the intersection of the electron trajectory on the surface, and E is the kinetic energy of the electrons. In addition, the transmission from solid to vacuum is modelled by a transmission coefficient that depends on the WF of the material [26].

A. Electron energy loss spectrum and secondary electron yield

Using the MC approach described above, we have calculated the reflection electron energy loss spectrum (REELS) [33] for different initial energies of the incident electrons (10, 20, 30, 50 keV), as shown in Fig. (5). Part of the electrons of the primary beam can be backscattered with the same energy as the incident energy and represents the so-called elastic (or lossless) peak, which typically also hides substructures due to electron-phonon scattering. To obtain a good signal-to-noise ratio, we performed all MC calculations with a total number of electrons equal to 10^{10} . The elastic peak is extremely bright in the figure and lies at the initial kinetic energy of the primary beam (black

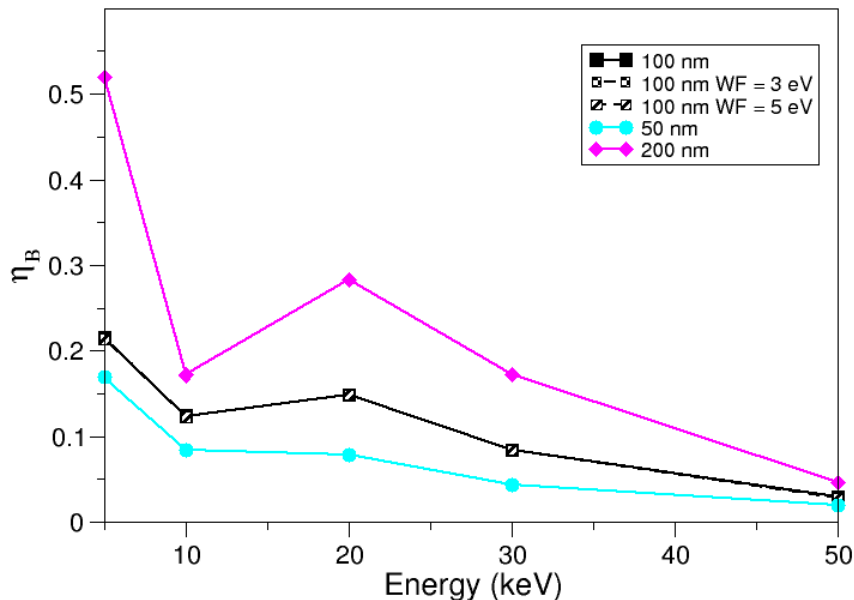


FIG. 6: Backscattering coefficient (η_B) for the electrons of the primary beam as a function of their initial kinetic energy (keV). The results are shown for three different sample thicknesses: 50 nm (cyan-coloured solid line), 100 nm (black solid line) and 200 nm (magenta-coloured solid line) for a WF value of 4.1 eV (pristine material). For the 100 nm layer, results with WF= 3.0 eV (black dotted-dashed line) and 5.0 eV (black dashed line) are also included to simulate the positively and negatively charged samples, respectively, and overlap with the pristine (WF=4.1 eV) case.

solid line for 10 keV kinetic energy, red line for 20 keV, green line for 30 keV and blue line for 50 keV). The energy loss spectra show several peaks reflecting the ELF lineshape. In Fig. (5), the inset image highlights the first 100 eV

of energy loss for an initial impact energy of 20 keV. The shoulders in the 20 keV REELS at 5, 8 and 12 eV from the elastic peak are directly related to single-particle excitations (Br $4p$ states \rightarrow Pb $6p$ states and Br $4p$ states \rightarrow Cs $6p$ states), which also occur in the ELF. The highest peak is at 22 eV away from the elastic peak, which is a mixed plasmon.

To investigate the effects of the film thickness on the reflected electrons, we also calculated the backscattering coefficient η_B (i.e. the fraction of backscattered electrons to total electrons) as a function of incident electron energies of 5, 10, 20, 30 and 50 keV. In Figure (6) we show the results for three CsPbBr₃ thin films of thickness 50 (cyan coloured line with full circles), 100 (black coloured line with full squares) and 200 nm (magenta coloured line with full diamonds). The backscattering coefficients for the CsPbBr₃ sample show a trend characterised by a relative minimum and a maximum that does not shift with increasing thickness. However, the number of reflected electrons increases with thickness and reaches a similar value for all thicknesses at an initial kinetic energy of the primary beam of 50 keV. The elastic peaks in Fig. (5) have an intensity trend similar to the η_B coefficient. This highlights the decisive contribution of elastic collision in reflection. To simulate perovskite samples that may be charged, we performed the MC calculations for a 100 nm thick layer for three different WF: 4.1 eV (i.e. the experimental value of the WF for the pristine material [34, 35]), 3 eV and 5 eV. The MC calculations for different WFs on a 100 nm slab (black, dotted and dashed lines) overlap almost perfectly with the results for the 4.1 eV WF and confirm that its value does not significantly influence the backscattering of the primary electrons.

Electron beams that hit a material can trigger the emission of secondary electrons by depositing their kinetic energy in the target. These electrons are emitted by the atoms of the solid as a result of inelastic interactions with the target, which may involve either the primary beam or other secondary electrons. The emission of secondary electrons is typically influenced by individual and collective charges, Auger decay, plasmons, phonons, trapping and charge density waves. Secondary electron emission is the primary contrast mechanism in an SEM and in SE imaging within the TEM. Secondary electron generation can also contribute to the charging of a sample which has implications on electron beam-induced damage mechanisms [4, 5, 7, 36]. In this context, the SE yield δ is defined as the ratio between the number of secondary electrons (reflected or transferred) and the total number of primary electrons. The secondary yield is thus defined per incident particle.

In Fig. (7) we show the yield of reflected secondary electrons determined for different initial energies of the primary electron beam of 1, 2, 5, 10, 20, 30, 50 keV for thicknesses of 50 (cyan-coloured line), 100 (black lines) and 200 nm (solid magenta-coloured line) and WF = 4.1 eV (pristine material). To investigate the dependence of the yield on the WF, calculations were also performed for WF = 3 eV (black dash-dotted line) and 5 eV (black dashed line) and 100 nm thickness.

The reflection yield of secondary electrons decreases with increasing initial kinetic energy, from which we can conclude that the low-energy primary electrons have a greater chance of producing the escaping secondary electrons immediately below the target surface. The secondary production dependent on the low energy impinging electron is confirmed by the similar δ trend independent of the sample thickness. In contrast to the analysis of primary electrons, the WF plays a fundamental role in increasing the production of secondary electrons: At low kinetic energy of the primary beam, a WF = 3 eV leads to an increased production of secondary electrons, while a WF = 5 eV attenuates them. This is particularly evident at the lowest energies (e.g. 2 and 5 keV) and confirms that impinging electrons with lower kinetic energy have a higher probability of emitting secondary electrons. In contrast, the electrons penetrate deep into the sample at the high energy of the primary beam (50 keV) and the generated secondary electrons cannot escape at the vacuum-target interface due to the numerous inelastic scatterings they suffer on their way out of the solid; in this case, the different WFs have little influence on the secondary reflection yield.

In Fig. (8) the secondary electron spectra are shown as a function of the initial kinetic energy of the primary beam equal to 1 (orange solid line), 2 (black solid line), 5 (red solid line), 10 (green solid line), 20 (blue solid line) and 50 keV (cyan solid line) for three different thicknesses of 50 (left), 100 (centre), 200 nm (right). The resulting secondary electrons are distributed over a range of 25 eV with a sustained peak of around 2.6 eV for all layer thicknesses and kinetic energies of the primary beam. The general shapes are consistent with the secondary kinetic energy spectra obtained by real-time TDDFT (RT-TDDFT) calculations for graphene, where a peak position at 3.5 eV [37] with a WF=4.56 eV was found, in semiconductor materials such as TiN, VN, GaAs, InAs, InSb, PbS by using Reverse MC approach [38], and with the analytical expression originally developed by Chung–Everhart [39] for metals, which relates the position of the secondary electron peak to the WF. The Chung–Everhart expression can be also used to estimate grossly the peak distributions for non-metals.

Considering the CsPbBr₃ WF = 4.1 eV and using the Chung–Everhart formula, the peak position is $4.1/3 \simeq 1.36$ eV ($\simeq 1.3$ eV below our estimate). Nevertheless, in our simulations, we confirm a red (blue) shift of the peak position by 0.3 eV for a WF of 3.0 eV (5.0 eV). At a thickness of 100 nm (centre panel of Fig. 8), the positively charged sample (WF = 3 eV, dotted-dashed line) enhances the intensity of the spectra of the kinetic energy of the secondary electrons, while the WF=5 eV (corresponding to negatively charged samples, dashed line) attenuates it. The conclusions drawn for the reflected secondary electron yield are confirmed by these results: (i) The more intense secondary electron

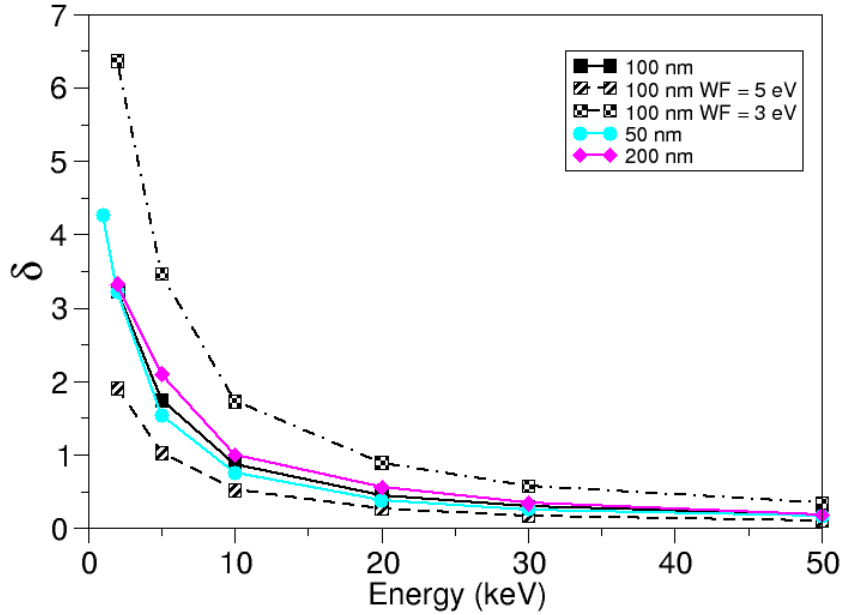


FIG. 7: Reflection yield of the secondary electrons (δ) as a function of the kinetic energy of the primary beam (keV). The results are shown for three different sample thicknesses and work functions: 50 nm (cyan-coloured solid line), 100 nm (black solid line) and 200 nm (magenta-coloured solid line) for WF= 4.1 eV (pristine material). For the 100 nm layer, results with WF= 3.0 eV (black dash-dotted line) and 5.0 eV (black dashed line) are also included.

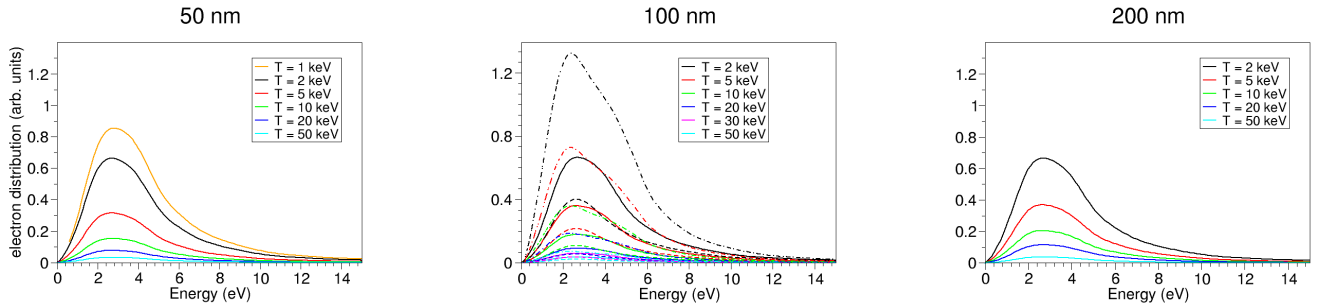


FIG. 8: Spectral distribution of the reflected secondary electrons (eV), parameterised for different initial kinetic energies of the primary electrons for three-layer thicknesses of 50 (left), 100 (centre) and 200 nm (right). For the 100 nm thick layer, the electron distribution was also calculated for a WF of 3.0 eV (dotted-dashed lines) and 5.0 eV (dashed lines), while the solid lines represent the pristine CsPbBr₃ (WF= 4.1 eV). The coloured lines represent the different initial kinetic energies of the primary beam of 1 (orange lines), 2 (black lines), 5 (red lines), 10 (green lines), 20 (blue lines), 30 (magenta lines) and 50 keV (cyan lines).

distributions are found for low kinetic energies of the primary electrons rather than for higher energies (e.g. 50 keV). (ii) The WFs influence the distributions of the secondary electron yield mainly at low kinetic energies of the primary electrons (with a maximum at 2.5 keV). (iii) The distributions are not significantly influenced by the thickness of the layer.

B. Transmission of the primary and secondary electrons.

The analysis carried out for the backscattered electrons is repeated for the primary and secondary electron transmission. In Fig. (9), the transmission coefficient (η_T) is plotted against the initial kinetic energies of the primary beam for three thicknesses. The number of transmitted primary electrons per incident particle is of course always

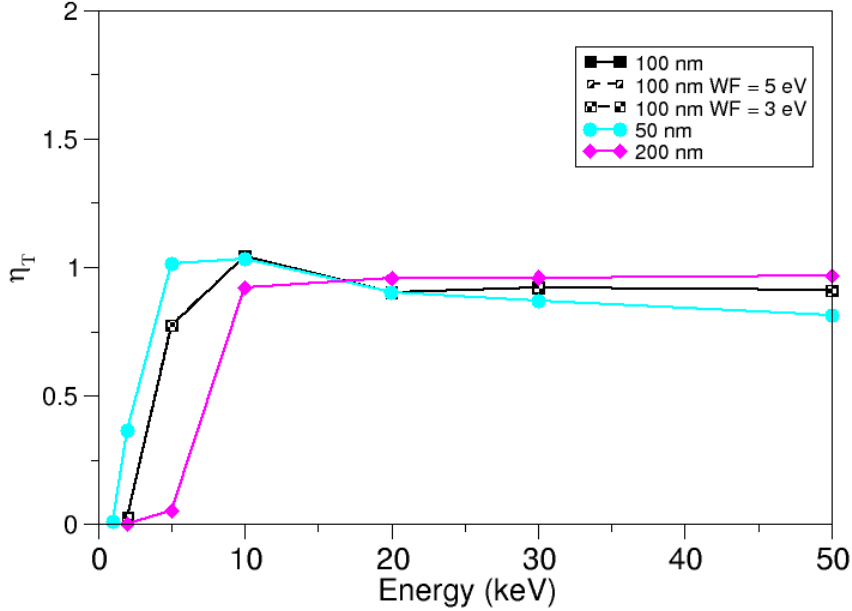


FIG. 9: Transmission coefficient (η_T) for the primary electrons as a function of the initial electron kinetic energy (keV). The results are shown for three different sample thicknesses and WF: pristine material (WF = 4.1 eV), 50 nm (cyan solid line), 100 nm (black solid line) and 200 nm (magenta solid line). Also shown are the results for a depth of 100 nm with WF = 3.0 eV (black dashed line) and 5.0 eV (black dashed line).

less than 1 at low kinetic energy, as a large fraction of the incident electrons are reflected. Nevertheless, the primary transmission coefficient saturates at a higher kinetic energy (10 keV).

In the case of 50 nm (cyan solid line), the primary electrons are almost completely transmitted at an incident energy of 2 keV. After 10 keV, however, η_T decreases slightly. In the 100 nm thick layer (black solid line), the transmission coefficient of the primary electrons shows a behaviour between 50 nm (cyan solid line) and 200 nm (magenta solid line), where $\eta_T \simeq 1$ is reached at 10 keV kinetic energy. Like the backscattering coefficient of the primary beam, the WF also does not influence the electron transmission for primary electrons, as was demonstrated in particular for the 100 nm thick layer (small and large squares).

The transmission coefficient of the secondary electrons as a function of the primary beam kinetic energy reported in Fig. (10) shows a maximum, whose position and intensity depend on the thickness: 2 keV for 50 nm (cyan solid line), 5 keV for 100 nm (black solid line) and 10 keV for 200 nm (magenta solid line).

We also note that the intensity of the maximum of δ_T decreases with increasing thickness and the WF also significantly influences the intensity of the transmitted secondary electrons, the higher the WF, the smaller δ_T . We attribute this result to the fact that the only secondary electrons that can escape are those that originate near the vacuum interface (opposite the entrance surface). This behaviour can be interpreted in light of the Fig. (11), where we present the distribution of transmitted secondary electrons as a function of origin depth. Furthermore, Fig. (11) shows that the number of secondary electrons produced initially increases when the energy of the primary electrons increases. However, this trend is reversed as soon as the energy exceeds a certain threshold value, which is determined by the thickness of the film. This leads to a saturation point at which a considerable number of electrons from the primary beam are transmitted and can therefore no longer contribute to the production of secondary electrons. This is also reflected in the thickness-dependent plateau in Fig. (9) for the transmission of the primary electrons. Finally, we find that the maximum of secondary electron transmission occurs at a depth of about 75 Å along the direction of incidence from the interface to the vacuum and the generation of secondary electrons is filtered out at low initial kinetic energy of the primary beam, e.g. the 2 keV distribution is most intense in a 50 nm thick layer, while it is attenuated in the 100 nm thick layer and suppressed in the 200 nm thick layer.

Finally, Figure (12) shows the energy distributions of the transmitted secondary electrons for different layer thicknesses parameterised with respect to the initial kinetic energy of the primary beam. Similar to the behaviour of the reflected secondary electrons, the energy spectra of the transmitted secondary electrons show a persistent peak around

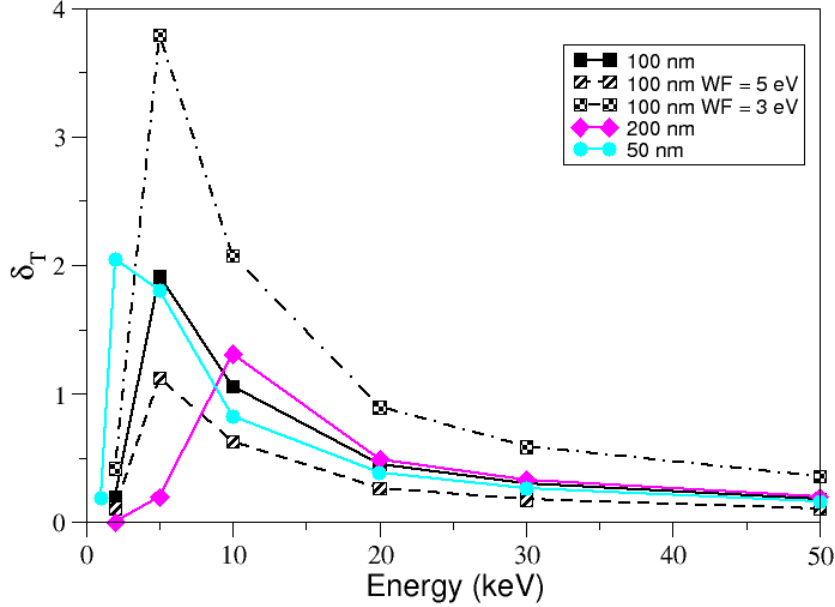


FIG. 10: Secondary electron transmission yield (δ_T) as a function of the initial kinetic energy of the primary beam (keV). The results are shown for three different sample thicknesses and work functions: pristine material (WF= 4.1 eV), 50 nm (cyan solid line), 100 nm (black solid line) and 200 nm (magenta solid line). The results for a depth of 100 nm with WF = 3.0 eV (black dashed line) and 5.0 eV (black dash-dotted line) are also shown.

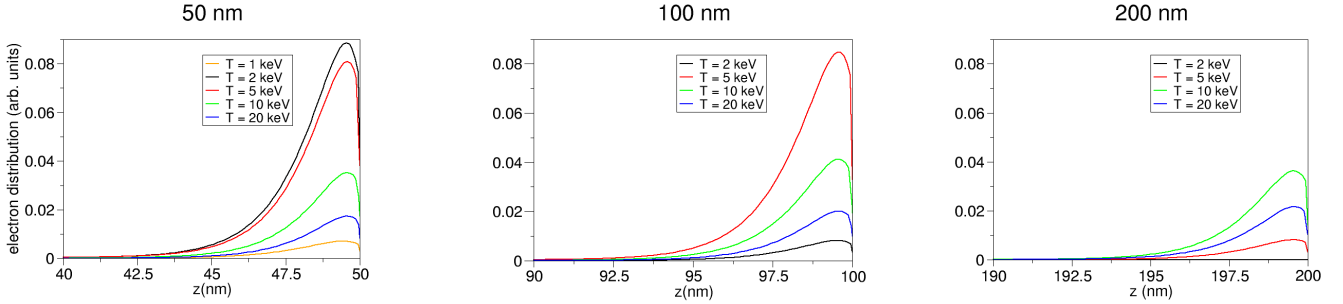


FIG. 11: Distribution of transmitted secondary electrons as a function of the origin depth (along z-axis, in nm), parameterised for different initial primary electron energies for slab thicknesses of 50 nm, 100 nm and 200 nm, respectively. The initial kinetic energies of the primary electron beam are $T = 1$ keV (orange lines), 2 keV (black lines), 5 keV (red lines), 10 keV (green lines) and 20 keV (blue lines).

2.6 eV, independent of the thickness and kinetic energy of the primary beam, with a tail reaching up to 20 eV. WF of 3 (5) eV increases (attenuates) the intensity of the peaks and produces a small red (blue) shift of the peak position, as demonstrated in the centre. The WF impacts the transmission yield of secondary electrons, even at a kinetic energy of 50 keV.

IV. DISCUSSION AND CONCLUSIONS

In this study, we theoretically investigated the scattering processes of high-energy primary and secondary electrons expected from Scanning Transmission Electron Microscopy (STEM) measurements of CsPbBr_3 . This was achieved through Monte Carlo (MC) simulations combined with first-principles LR-TDDFT calculations for Electron Loss Function (ELF).

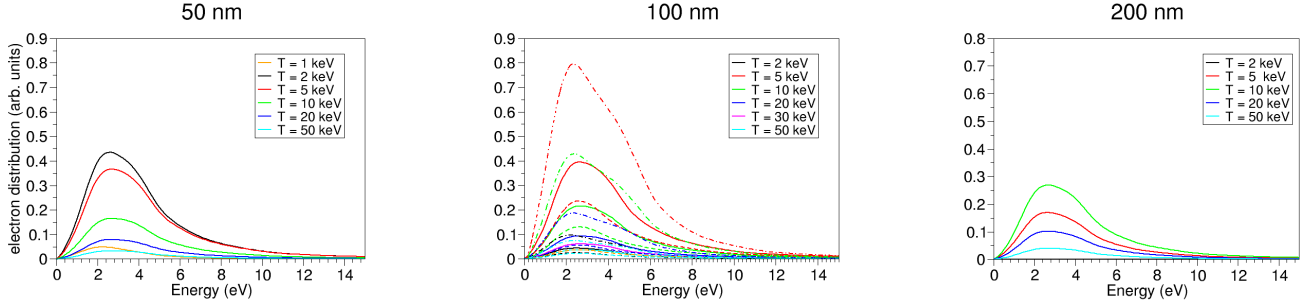


FIG. 12: Energy spectra of transmitted secondary electrons as a function of emission kinetic energy (eV) for different initial primary electron energies for three slab thicknesses (50 nm, 100 nm and 200 nm). For the 100 nm slab, the electron distribution was also calculated with a WF of 3.0 eV (dotted-dashed lines) and 5.0 eV (dashed lines), while for the original CsPbBr₃ the WF is 4.1 eV (solid lines). The initial kinetic energies of the primary beam are $T = 1$ keV (orange lines), 2 keV (black lines), 5 keV (red lines), 10 keV (green lines), 20 keV (blue lines), 30 keV (magenta lines) and 50 keV (cyan lines).

For the first time, we calculated the LR-TDDFT ELF and the Inelastic Mean Free Path (IMFP) for bulk CsPbBr₃ to support these simulations. We particularly focused on quantifying the reflection and transmission for backscattering and secondary electron yield (SEY) processes, as well as the energy distributions of the emitted secondary electrons.

Our findings showed that, for backscattering processes involving primary electrons, there is nearly no dependence on the WF, with a transmission coefficient approaching one at input energies of 10 keV. However, the situation changes significantly for the reflection and transmission of secondary electrons. The WF plays a critical role in the production of these outgoing electrons, although its influence diminishes at higher energies.

In terms of transmission, the observed peaks are dependent on both the thickness of the material and the initial kinetic energy of the primary electrons. Outgoing secondary electrons are most likely to be emitted when they are generated within the last 10 nm of the nanolayer. Therefore, the kinetic energy of the incoming electrons must be carefully balanced; it should be high enough to generate secondary electrons without releasing too much energy and low enough to prevent the generation of secondaries too deeply within the sample.

These results contribute to a better understanding of the transmission and reflection characteristics of primary and secondary electrons, ultimately aiding in the optimization of STEM experimental measurements.

ACKNOWLEDGMENTS

This work was supported by the Ada Lovelace Centre.

The authors acknowledge the use of the ARCHER2 (via the UK Car-Parrinello Consortium, EP/X035891/1) and STFC-SCARF HPC facilities.

The authors receiving funds from grant agreement No. 10104665 acknowledge the European Union.

P.E.T. thanks Dr J. Jackson for assistance with the Questaal calculations and Dr I. Scivetti for his help with Archer2.

Appendix A: Drude-Lorentz method

The inelastic scattering cross-section is derived from the ELF in the entire spectrum of excitation energies (ω) and momentum transfers q . Performing ab initio calculations of the ELF over a wide energy range is often prohibitively expensive due to the complex computational requirements resulting from the inclusion of multiple electronic transitions to excited states. While first-principles methods can effectively calculate the ELF for energies below 100 eV, these calculations had to be extended to higher excitation energies by using experimental NIST X-ray atomic data (TDDFT-NIST) up to 400 keV [30].

The TDDFT-NIST ELF was first fitted using the ALC_SUTOR suite [40], which uses nonlinear least squares minimisation *lmfit* [41]. We used 34 Drude-Lorentz oscillators with a momentum-dependent broadening parameter γ_i as follows:

$$\text{Im} \left\{ \frac{-1}{\bar{\epsilon}(\mathbf{q} = \mathbf{0}, \omega)} \right\} = \sum_i \frac{A_i \gamma_i \omega}{(\omega_i^2 - \omega^2)^2 + (\gamma_i \omega)^2}, \quad (\text{A1})$$

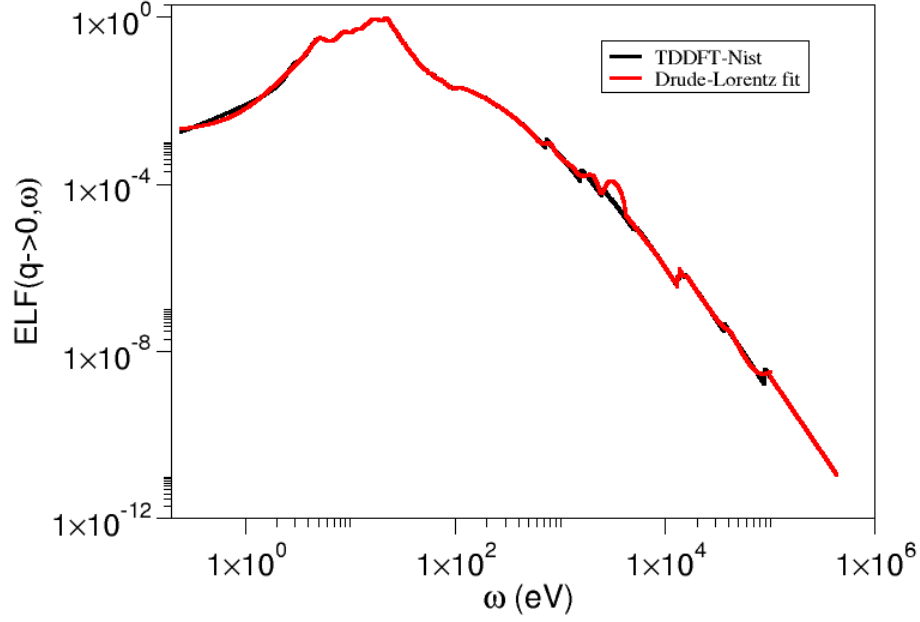


FIG. 13: Drude-Lorentz fit (black line) of the TDDFT-NIST [30] ELF (red line).

where A_i represents the intensity of the transition. The friction damping parameter γ_i takes into account the momentum dispersion of the i th electronic interband and intraband excitation in the valence and conduction bands, which is characterised by a transition energy ω_i according to the following formula [42]:

$$\begin{aligned}\omega_i(q) &= \sqrt{\omega_i^2 + (12/5)E_f \cdot q^2/2 + q^4/4} \\ \gamma_i(q) &= \sqrt{\gamma_i + q^2/2 + q^4/4}\end{aligned}\tag{A2}$$

To include the electronic excitations of the inner shells in the ELF calculation, we have additionally used 10 Fano functions and 4 power-law functions that accurately reproduce the sharp edges associated with the core excitations.

The result of this fitting procedure is shown in Fig. 13. For details on different methods to extend the ELF beyond the optical limit, see Ref. [26].

-
- [1] A. Rivacoba, N. Zabala, and J. Aizpurua, Image potential in scanning transmission electron microscopy, *Progress in Surface Science* **65**, 1 (2000).
 - [2] P. D. Nellist, Scanning transmission electron microscopy, in *Springer Handbook of Microscopy*, edited by P. W. Hawkes and J. C. H. Spence (Springer International Publishing, Cham, 2019) pp. 49–99.
 - [3] S. Taioli, S. Simonucci, L. Calliari, and M. Dapor, Electron spectroscopies and inelastic processes in nanoclusters and solids: Theory and experiment, *Physics Reports* **493**, 237 (2010).
 - [4] B. Plotkin-Swing, J. Martis, C. Su, M. T. Hotz, N. Dellby, T. Radlička, O. L. Krivanek, and T. C. Lovejoy, Atomic resolution secondary electron imaging of top and bottom surfaces, *Microscopy and Microanalysis* **30**, ozae044.731 (2024), https://academic.oup.com/mam/article-pdf/30/Supplement_1/ozae044.731/58669239/ozae044.731.pdf.
 - [5] O. Dyck, J. L. Swett, C. Evangelini, A. R. Lupini, J. Mol, and S. Jesse, Contrast mechanisms in secondary electron e-beam-induced current (seebic) imaging, *Microscopy and Microanalysis* **28**, 1567–1583 (2022).
 - [6] M. L. San Gabriel, C. Qiu, D. Yu, T. Yaguchi, and J. Y. Howe, Simultaneous secondary electron microscopy in the scanning transmission electron microscope with applications for in situ studies, *Microscopy* **73**, 169 (2024), <https://academic.oup.com/jmicro/article-pdf/73/2/169/57186962/dfae007.pdf>.
 - [7] H. Suzuki, Z. Akase, K. Niitsu, T. Tanigaki, and D. Shindo, Secondary electron effect on electron beam induced charging of sio2 particle analyzed by electron holography, *Microscopy* **66**, 167 (2017).

- [8] M. Dapor, M. Ciappa, and W. Fichtner, Monte Carlo modeling in the low-energy domain of the secondary electron emission of polymethylmethacrylate for critical-dimension scanning electron microscopy, *Journal of Micro/Nanolithography, MEMS, and MOEMS* **9**, 023001 (2010).
- [9] S. Taioli, M. Dapor, F. Dimiccoli, M. Fabi, V. Ferroni, C. Grimani, M. Villani, and W. J. Weber, The role of low-energy electrons in the charging process of lisa test masses, *Classical and Quantum Gravity* **40**, 075001 (2023).
- [10] R. F. Egerton, *Electron Energy-Loss Spectroscopy in the Electron Microscope* (Springer, New York, Dordrecht, Heidelberg, London, 2011).
- [11] Z. Li, J. Gong, B. Da, J. Tóth, K. Tórkési, R. Zeng, and Z. J. Ding, Improved reverse monte carlo analysis of optical property of fe and ni from reflection electron energy loss spectroscopy spectra, *Scientific Reports* **13** (2023).
- [12] P. de Vera, I. Abril, and R. Garcia-Molina, Electronic cross section, stopping power and energy-loss straggling of metals for swift protons, alpha particles and electrons, *Front. Mater.* **10**, 1249517 (2023).
- [13] S. Shi, Y. Wang, S. Zeng, Y. Cui, and Y. Xiao, Surface regulation of csppbr₃ quantum dots for standard blue-emission with boosted plqy, *Advanced Optical Materials* **8**, 10.1002/adom.202000167 (2020).
- [14] S. Wang, C. Bi, J. Yuan, L. Zhang, and J. Tian, Original core-shell structure of cubic csppbr₃ amorphous csppbr₃ perovskite quantum dots with a high blue photoluminescence quantum yield of over 80%, *ACS ENERGY LETTERS* **3**, 245 (2018).
- [15] J.-S. Yao, J. Ge, B.-N. Han, K.-H. Wang, H.-B. Yao, H.-L. Yu, J.-H. Li, B.-S. Zhu, J.-Z. Song, C. Chen, Q. Zhang, H.-B. Zeng, Y. Luo, and S.-H. Yu, Ce₃-doping to modulate photoluminescence kinetics for efficient csppbr₃ nanocrystals based light-emitting diodes, *Journal of the American Chemical Society* **140**, 3626 (2018).
- [16] H. Guan, S. Zhao, H. Wang, D. Yan, M. Wang, and Z. Zang, Room temperature synthesis of stable single silica-coated csppbr₃ quantum dots combining tunable red emission of ag-in-zn-s for high-cri white light-emitting diodes, *Nano Energy* **67**, 10.1016/j.nanoen.2019.104279 (2020).
- [17] S. Wei, Y. Yang, X. Kang, L. Wang, L. Huang, and D. Pan, Room-temperature and gram-scale synthesis of csppbx₃ (x = cl, br, i) perovskite nanocrystals with 50-85% photoluminescence quantum yields, *Chemical Communications* **52**, 7265 (2016).
- [18] Z.-J. Yong, S.-Q. Guo, J.-P. Ma, J.-Y. Zhang, Z.-Y. Li, Y.-M. Chen, B.-B. Zhang, Y. Zhou, J. Shu, J.-L. Gu, L.-R. Zheng, O. M. Bakr, and H.-T. Sun, Doping-enhanced short-range order of perovskite nanocrystals for near-unity violet luminescence quantum yield, *Journal of the American Chemical Society* **140**, 9942 (2018).
- [19] D. Han, K. Yang, C. Bai, F. Chen, Z. Sun, Y. Wang, H. Ji, Z. Yang, and X. Tang, Thermal and chemical durability of metal halide perovskite csppbr₃ single crystals, *Chemical Engineering Journal* **475**, 10.1016/j.cej.2023.146209 (2023).
- [20] C. Bi, Z. Yao, X. Sun, X. Wei, J. Wang, and J. Tian, Perovskite quantum dots with ultralow trap density by acid etching-driven ligand exchange for high luminance and stable pure-blue light-emitting diodes, *Advanced Materials* **33**, 10.1002/adma.202006722 (2021).
- [21] L. Protesescu, S. Yakunin, S. Kumar, J. Bar, F. Bertolotti, N. Masciocchi, A. Guagliardi, M. Grotevent, I. Shorubalko, M. I. Bodnarchuk, C.-J. Shih, and M. V. Kovalenko, Dismantling the “red wall” of colloidal perovskites: Highly luminescent formamidinium and formamidinium-cesium lead iodide nanocrystals, *acs nano* **11**, 3119 (2017).
- [22] M. Ezzeldien, S. Al-Qaisi, Z. A. Alrowaili, M. Alzaid, E. Maskar, A. Es-Smairi, T. V. Vu, and D. P. Rai, Electronic and optical properties of bulk and surface of csppbr₃ inorganic halide perovskite a first principles dft 1/2 approach, *Scientific Reports* **11**, 20622 (2021).
- [23] B. Yang and K. Han, Charge-carrier dynamics of lead-free halide perovskite nanocrystals, *Accounts of Chemical Research* **52**, 3188 (2019).
- [24] P. Zeng, X. Ren, L. Wei, H. Zhao, X. Liu, X. Zhang, Y. Xu, L. Yan, K. Boldt, T. A. Smith, and M. Liu, Control of hot carrier relaxation in csppbr₃ nanocrystals using damping ligands, *Angewandte Chemie-International edition* **61**, 10.1002/anie.202111443 (2022).
- [25] R. H. Ritchie, Plasma losses by fast electrons in thin films, *Phys. Rev.* **106**, 874 (1957).
- [26] S. Taioli and M. Dapor, Advancements in secondary and backscattered electron energy spectra and yields analysis: From theory to applications, *Surface Science Reports* **80**, 100646 (2024).
- [27] M. Rodová, J. Brožek, K. Knížek, and K. Nitsch, Phase transitions in ternary caesium lead bromide, *Journal of Thermal Analysis and Calorimetry* **71**, 667 (2003).
- [28] I. Timrov, N. Vast, R. Gebauer, and S. Baroni, turboeels—a code for the simulation of the electron energy loss and inelastic x-ray scattering spectra using the liouville–lanczos approach to time-dependent density-functional perturbation theory, *Computer Physics Communications* **196**, 460 (2015).
- [29] M. Marques and E. Gross, Time-dependent density functional theory, *Annu. Rev. Phys. Chem.* **55**, 427 (2004).
- [30] S. Seltzer, X-ray form factor, attenuation and scattering tables, nist standard reference database 66 (1995).
- [31] F. Salvat, A. Jablonski, and C. J. Powell, ELSEPA—Dirac partial-wave calculation of elastic scattering of electrons and positrons by atoms, positive ions and molecules, *Comp. Phys. Comm.* **165**, 157 (2005).
- [32] M. Dapor, *Transport of Energetic Electrons in Solids. Computer Simulation with Applications to Materials Analysis and Characterization*, 4th ed., Springer Tracts in Modern Physics, Vol. 290 (Springer Nature Switzerland AG, 2023).
- [33] Z. Li, J. M. Gong, B. Da, J. Tóth, K. Tórkési, R. G. Zeng, and Z. J. Ding, Improved reverse monte carlo analysis of optical property of fe and ni from reflection electron energy loss spectroscopy spectra, *Scientific Reports* **13**, 12480 (2023).
- [34] J. Endres, D. A. Egger, M. Kulbak, R. A. Kerner, L. Zhao, S. H. Silver, G. Hodes, B. P. Rand, D. Cahen, L. Kronik, and A. Kahn, Valence and conduction band densities of states of metal halide perovskites: A combined experimental–theoretical study, *The Journal of Physical Chemistry Letters* **7**, 2722 (2016).
- [35] F. Liu, S. Sidhik, M. A. Hoffbauer, S. Lewis, A. J. Neukirch, V. Pavlenko, H. Tsai, W. Nie, J. Even, S. Tretiak, P. M. Ajayan, M. G. Kanatzidis, J. J. Crochet, N. A. Moody, J.-C. Blancon, and A. D. Mohite, Highly efficient photoelectric

- effect in halide perovskites for regenerative electron sources, *Nature Communications* **12**, 673 (2021).
- [36] R. Egerton, Radiation damage and nanofabrication in tem and stem, *Microscopy Today* **29**, 56–59 (2021).
- [37] Y. Yao, A. Kononov, A. Metzloff, A. Wucher, L. Kalkhoff, L. Breuer, M. Schleberger, and A. Schleife, Nonequilibrium dynamics of electron emission from cold and hot graphene under proton irradiation, *Nano Letters* **24**, 5174 (2024).
- [38] A. Hussain, L. H. Yang, Y. B. Zou, S. F. Mao, B. Da, H. M. Li, and Z. J. Ding, Theoretical calculations of the mean escape depth of secondary electron emission from compound semiconductor materials, *Journal of Applied Physics* **127**, 125304 (2020), https://pubs.aip.org/aip/jap/article-pdf/doi/10.1063/1.5144721/15244163/125304_1_online.pdf.
- [39] M. S. Chung and T. E. Everhart, Simple calculation of energy distribution of low-energy secondary electrons emitted from metals under electron bombardment, *Journal of Applied Physics* **45**, 707 (1974).
- [40] Alc_sutor, https://github.com/stfc/ALC_SUTOR.
- [41] lmfit, <https://lmfit.github.io/lmfit-py/>.
- [42] A. Pedrielli, N. M. Pugno, M. Dapor, and S. Taioli, In search of the ground-state crystal structure of ta₂o₅ from ab initio and monte carlo simulations, *Computational Materials Science* **216**, 111828 (2023).